Check for updates

Promoted glucose electrooxidation at Ni(OH)₂/graphene layers exfoliated facilely from carbon waste material

Ahmed M. Abdelrahim, [ID] Muhammad G. Abd El-Moghny, [ID] * Mohamed E. El-Shakre and Mohamed S. El-Deab [ID] *

Nowadays, the glucose electro-oxidation reaction (GOR) is considered one of the most important solutions for environmental pollution. The GOR is the anodic reaction in direct glucose fuel cells and hybrid water electrolysis. In this study, the GOR is boosted using a carbon support modified with Ni(OH)₂ as a non-precious catalyst. The carbon support, with *in situ* generated graphene nanosheets having a large surface area, grooves, and surface functional groups, is prepared *via* a simple electrochemical treatment of the carbon rods of an exhausted zinc-carbon battery. Ni(OH)₂ is electrodeposited on the surface of the functionalized exfoliated graphite rod (FEGR) *via* the dynamic hydrogen bubbling technique (DHBT) and tested for GOR. The thus-prepared Ni(OH)₂/FEGR electrode is characterized by SEM, mapping EDX, HR-TEM, XRD, and XPS characterization tools. Ni(OH)₂/FEGR displays an onset potential of 1.23 V *vs.* the reversible hydrogen electrode (RHE) and attains high current densities at lower potentials. Additionally, Ni(OH)₂/FEGR showed prolonged stability toward GOR by supporting a constant current over a long electrolysis time. The enhanced catalytic performance is attributed to the superb ionic and electronic conductivity of the catalyst. Importantly, ionic conductivity increased, due to (i) a large surface area of *in situ* generated graphene layers, (ii) enhanced distribution of active material during deposition using DHBT, and (iii) increased hydrophilicity of the underlying substrate. Therefore, the Ni(OH)₂/FEGR electrode can be used efficiently for GOR as a low-cost catalyst, achieving low onset potential and high current densities at low potentials.

1. Introduction

Recently, renewable energy technologies have attracted great attention due to the rapid depletion of fossil fuels and their limited resources, together with the related environmental drawbacks. Thus, an urgent need has emerged to increase the contribution of renewable energy sources (*e.g.*, wind, solar and geothermal energy, fuel cells, *etc.*) to replace traditional fossil fuels.[1–5] Nowadays, glucose solves many environmental problems *via* its use in fuel cells and hydrogen production. In this regard, direct glucose fuel cells (DGFCs) stand among the most efficient electrical energy conversion systems due to their unique advantages, *i.e.* glucose (as a fuel) is naturally abundant, cheap, non-toxic, easy to store and transport, eco-friendly, and high energy (glucose release 2.87 MJ mol⁻¹ upon complete oxidation).[6–9] Also, glucose electro–oxidation reaction (GOR) is used in hybrid water electrolysis instead of the oxygen evolution reaction (OER) to produce hydrogen at low cell voltage.[10–13]

Recently, the usage of non-precious transition metal-based catalysts such as Cu, Ni, and Co toward GOR is a goal of research to replace the high-cost-based metals such as Pt and Au.[14–16] Among the various catalysts based on transition metals, Ni(OH)₂ materials had been proven to be promising catalyst for GOR due to their unique layered structure with large interlayer spacing that allows the electrolyte diffusion within the catalyst layers resulting in a boosted catalytic activity.[17–20] Glucose can be oxidized into gluconolactone in the presence of Ni(OH)₂ according to the following eqn (1) and (2):[14]

$$Ni(OH)_2 + OH^- \rightarrow NiOOH + H_2O + e^- \quad (1)$$

$$2NiOOH + Glucose \rightarrow gluconolactone + 2Ni(OH)_2 \quad (2)$$

Interestingly, Ni(OH)₂ has two polymorphic crystal structures, α-Ni(OH)₂ phase with hydrotalcite-like structure and β-Ni(OH)₂ with brucite-like structure (see Scheme 1).[21–23] α-Ni(OH)₂ has a higher *d*-spacing value with the turbostratically crystallized structure due to the presence of the water molecules and/or anions (*e.g.* SO_4^{2-}, Cl^-, NO_3^-, and CH_3COO^-) between the hydroxide layers.[21–23] β-Ni(OH)₂ has a lower theoretical oxidation potential than α-Ni(OH)₂ and thus has higher

Department of Chemistry, Faculty of Science, Cairo University, Cairo, Egypt. E-mail: mugamal@cu.edu.eg; gmohamd@sci.cu.edu.eg; msaada@cu.edu.eg; msaada68@yahoo.com

catalytic activity toward GOR into gluconolactone, as demonstrated by El-Nagar.[14] However, it is sometimes found that the α-Ni(OH)$_2$ showed higher catalytic activity than β-NiOOH because of its morphology and the large d-spacing that facilitates the access of electrolyte ions to its active sites thus being converted to the γ-NiOOH which oxidizes the glucose. Guo-Xiu Tong[24] prepared α-Ni(OH)$_2$ with flower-like morphology with high surface area and higher catalytic activity toward GOR than β-Ni(OH)$_2$ microsphere. Also, Pan lu[25] proved that rose-like nanostructured α-Ni(OH)$_2$ prepared by a hydrothermal method has enhanced the catalytic activity toward GOR.

Although Ni(OH)$_2$ has a higher catalytic behavior toward GOR, it has some drawbacks such as low electrical conductivity ($\sim 10^{-17}$ S cm^{-1}), low ionic conductivity, and low durability. Therefore, research efforts are directed to investigate substrate materials, which act as catalyst support, characterized by a high electrical conductivity, and high surface area with a porous structure to overcome these problems.[15,26]

Carbon-based materials are promising catalyst support due to their unique characteristics such as (i) high surface area and porous structure, (ii) high electronic conductivity, and (iii) wide operating potential window which is a very important parameter for the electrode performance, and (iv) excellent physical, mechanical and electrochemical properties.[27–31] Graphene is one of the most important used carbon-based materials in energy devices due to its unrivaled advantages, unique 2D structure with a huge gravimetric surface area (~ 2600 m^2 g^{-1}), ultra-high electrical conductivity, very high charge carrier mobility ($\sim 200\,000$ cm^2 V^{-1} s^{-1}), excellent mechanical and physical properties, outstanding thermal conductivity, and being non-toxic material.[29,30,32–36]

Therefore, the researchers were motivated to prepare high-quality graphene using different methods; micromechanical exfoliation, thermal decomposition of SiC, chemical vapor deposition (CVD), and chemical and electrochemical exfoliation. However, micromechanical exfoliation displays high-quality graphene production unless this method is not suitable for large-scale productions. CVD is a well-known method to produce graphene on a large scale, but this method requires a highly expensive substrate during the preparation process which limits its use in commercial applications.[30,32,37,38] On the other hand, Hummer developed a cost-effective method based on chemical exfoliation replacing the high-cost CVD and thermal decomposition methods. Hummers' method is based on two sequential steps. Firstly, the production of graphene oxide (GO) *via* exfoliation of graphite in the strong oxidants and acids followed by the reduction of the produced GO using chemical or thermal way.[30,38] Interestingly, the complete exfoliation Hummers' method has many disadvantages such as being sophisticated and time-consuming, using harsh materials, and requiring a binder which hinders the catalyst performance by increasing resistance rather than the binder's high cost.[27,33,34,37]

To solve this issue, many researchers have proposed the partial exfoliation of graphite using an electrochemical oxidation setup. Advantageously, electrochemical partial exfoliation has many advantages such as being a simple, safe, controllable, binder-free, low-cost, and eco-friendly method. This method produces functionalized graphene sheets as top layers electrically connected to the graphite (bottom layer). The resulting highly conductive three-dimensional functionalized exfoliated graphene can be used as excellent support to accommodate the
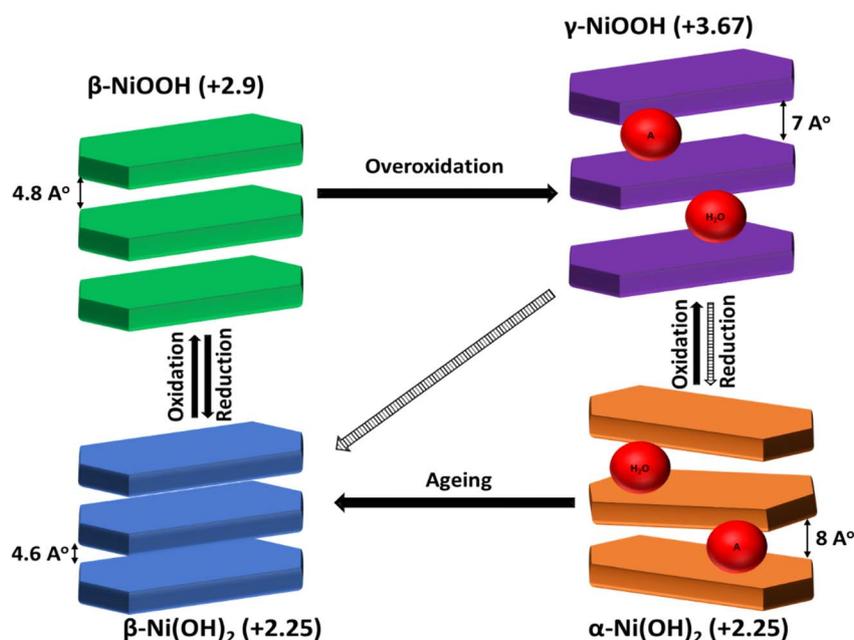
Scheme 1 Schematic illustration of Ni(OH)$_2$/NiOOH phase transformations (Bode diagram). Note that the A represents the possible anions (*e.g.*, SO$_4^{2-}$, Cl$^-$, NO$_3^-$, and CH$_3$COO$^-$) that can be incorporated between the layers of hydroxide during synthesis.[21,42]

redox-active materials to enhance their electrical conductivity.[28,29,32]

Over and above, preparation techniques play an essential role in determining the catalytic activity of the electrode material. Several techniques have been reported to synthesize metal-based materials. The electrochemical deposition technique has attracted much attention due to being simple, controllable, cost-effective, and free binder method. Specifically, the dynamic hydrogen bubbling technique (DHBT) is considered a promising method for electrodeposition due to being simple and fast, producing high surface area by developing a porous structure, and being controllable.[39–41]

Therefore, the current research focuses on the preparation of non-precious catalysts on the surface of supporting materials with characteristic properties. Interestingly, seeking supporting materials with characteristic properties from waste materials is still challenging.

Herein, graphene layers with a large surface area are prepared from waste material *via* a facile method. Electrochemical partial exfoliation of the recycled graphite rod (RGR) is done to produce the functionalized exfoliated graphite rod (FEGR) to act as excellent support for $Ni(OH)_2$. The FEGR boosted the catalytic activity of $Ni(OH)_2$ towards GOR. The preparation of catalyst, $Ni(OH)_2$/FEGR, has many advantages such as being a simple, safe, controllable, low-cost, binder-free, and eco-friendly method. Additionally, the FEGR support enhances the hydrogen evolution reaction during electrodeposition by DHBT providing homogeneous distribution of active sites. As a result, $Ni(OH)_2$/FEGR boosted the GOR by displaying a lower onset potential (1.23 V *vs.* RHE) and by attaining high current densities at a lower potentials. Also, $Ni(OH)_2$/FEGR electrode displays excellent stability toward GOR. Additionally, at any current density, the potential of the GOR is much lower than that of OER. Therefore, the boosted GOR on the surface of the $Ni(OH)_2$/FEGR can be used in many applications such as DGFCs, and hybrid water electrolysis. The superior performance of $Ni(OH)_2$/FEGR catalyst is attributed to (a) the increased exposed active sites, (b) the enhanced diffusion of the electrolytes by increasing the surface hydrophilicity, (c) the enhanced electronic conductivity of the catalyst, and (d) the superb stability.

2. Experimental

2.1. Chemicals and electrodes preparation

2.1.1 Chemicals. All the used chemicals were of analytical grade (purchased from Sigma Aldrich and Merck, Germany) and were used as received without any further purification. All solutions were prepared using second distilled water.

2.1.2 Electrodes preparation. Firstly, RGR with a 4 mm diameter is obtained from the exhausted zinc–carbon batteries with a nominal voltage of 1.5 V. RGR is cleaned by performing the following steps: mechanically polishing the surface of the RGR to remove any big residual particles, followed by three minutes of immersion in boiling distilled water while being continuously stirred to remove any fine residual particles. In a three-electrode configuration cell (RGR) served as the working

electrode (immersed length 1 cm), graphite rod, and saturated calomel electrode (SCE) used as the counter and reference electrodes, respectively, the FEGR is made using a straightforward electrochemical anodic oxidation step that involves applying an oxidation potential of +2 V in a solution containing 1 M H_2SO_4 for 10 minutes. Secondly, $Ni(OH)_2$/RGR and $Ni(OH)_2$/FEGR electrodes were prepared by the following procedure:

(1) Electrodeposition of Ni metal using DHBT. During the deposition of Ni, the RGR and FEGR are used as working electrodes, and the graphite rod and SCE are serving as the counter and reference electrodes, respectively. The deposition was done by allowing the passage of 20 Coulombs (C) at −2 V in the aqueous solution containing 0.1 M $NiCl_2$ and 1 M NH_4Cl at room temperature (25 °C ± 1).

(2) Electrochemical passivation of the obtained Ni metal is carried out in an aqueous solution of 0.5 M NaOH potentiodynamically by cycling the potential from −0.1 to 0.7 V *vs.* SCE for 30 cycles using a potential scan rate of 50 mV s^{-1}.

2.2. Materials characterization

Surface morphology, chemical composition, and structure of the various modified electrodes were examined by field emission scanning electron microscope (FE-SEM, QUANTA FEG 250) coupled with an energy dispersive X-ray spectrometer (EDX) unit and high-resolution transmission electron microscopy (HR-TEM) (JEOL, JEM-2100, Tokyo, Japan). X-ray photoelectron spectroscopy (XPS), using monochromatic X-ray Al Kα radiation, Thermo Fisher Scientific. Additionally, the crystalline structures were characterized using X-ray diffraction (XRD) with Cu Kα radiation, STOE STADI. Inductively coupled plasma-optical emission spectrometer (ICP-OES) measurements were carried out (ICP-OES Optima 2000 DV PerkinElmer Microwave CRM Mars 5) to obtain the amount of active material on each electrode.

2.3. Electrochemical measurements

The electrochemical measurements were investigated using a three-electrode cell configuration at room temperature (25 °C ± 1) and a Biologic potentiostat (model VSP-300). Electrocatalytic performance was measured *via*, cyclic voltammetry (CV), linear sweep voltammetry (LSV), chronoamperometry (CA), and electrochemical impedance spectroscopy (EIS) (from 100 kHz to 20 mHz) in a 0.5 M NaOH aqueous solution containing a known amount of glucose.

3. Results and discussion

The surface morphology was inspected using SEM analysis. From Fig. 1, while the surface of RGR displays smooth surface with small percentage of defects (composed mainly of carbon and small percentage of oxygen) (see Fig. 1A), the FEGR is characterized by the presence of exfoliated graphene layers and uniformly distributed grooves atop the graphite rod's surface (see Fig. 1B). Also, as a result of the oxidation, the FEGR displays highly distributed oxygenated functional groups (see Fig. 1B, elemental mapping EDX analysis). Because of the characteristic
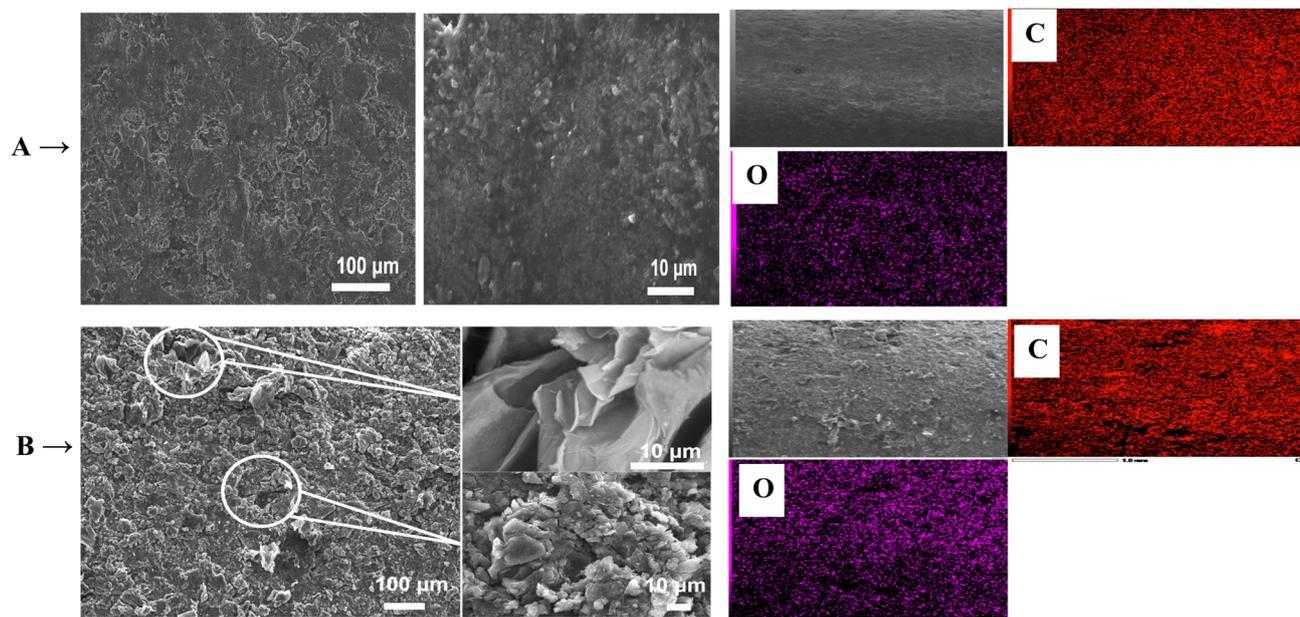
Fig. 1 SEM images with different magnifications and elemental mapping EDX analysis of (A) RGR support, and (B) FEGR support.
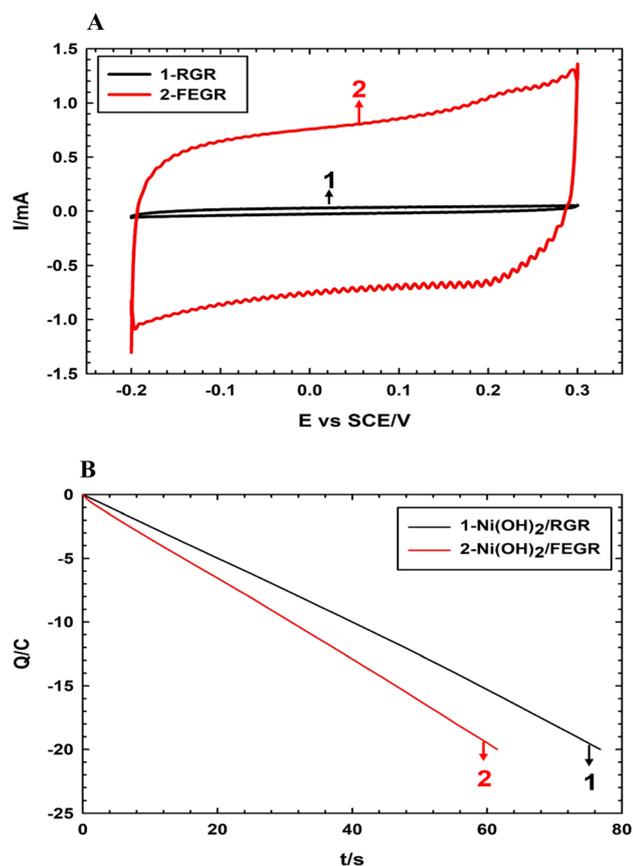

Fig. 2 (A) CVs obtained at RGR and FEGR supports measured in 0.5 M NaOH solution at a potential scan rate of 100 mV s^{-1}. (B) Controlled potential coulometry recorded at −2 V *vs.* SCE during electrodeposition of Ni(OH)$_2$ films on the surface of FEGR (red line) and RGR (black line) supports.

morphology of FEGR, it can be used as promising support to accommodate a large number of active materials that can be used efficiently toward GOR.

Firstly, the enhancement of the FEGR support can be obvious by providing a large surface area that can be available to ingest the large quantity of catalyst layer. As shown in Fig. 2A, the calculated specific capacitance (C_s) of FEGR using eqn (3) is 5.5 mF cm^{-2} which is greater than the C_s of RGR (0.21 mF cm^{-2}) by 26 times.

$$C_s = \frac{\int I \, dt}{S \Delta V} \tag{3}$$

where C_s is the specific capacitance in F cm^{-2}, S is the area of the electrode in cm^2, $\int I \, dt$ is the integrated oxidation or reduction current–potential area divided by the potential scan rate, and ΔV is the operating potential window in V.[21,43]

The high specific capacitance of the FEGR support is reflected in, the large adsorption capacity of this large activated electrode's surface to ingest a large number of electrolyte species by supplying a rough surface, a large number of the homogeneous-distributed grooves on the surface of the electrode, in addition to the large produced number of expanded graphene sheets.

Secondly, the FEGR electrode minimizes the coagulation of the catalyst species during its electrodeposition using the DHBT. During metal electrodeposition (see eqn (4)) using DHBT, H$_2$ bubbles are formed from the electrolysis of water and ammonium chloride due to higher overpotential applied according to eqn (5) and (6), respectively, which bubbles off the growing deposited metal (eqn (4)), disrupting the growth mechanism.[44,45]
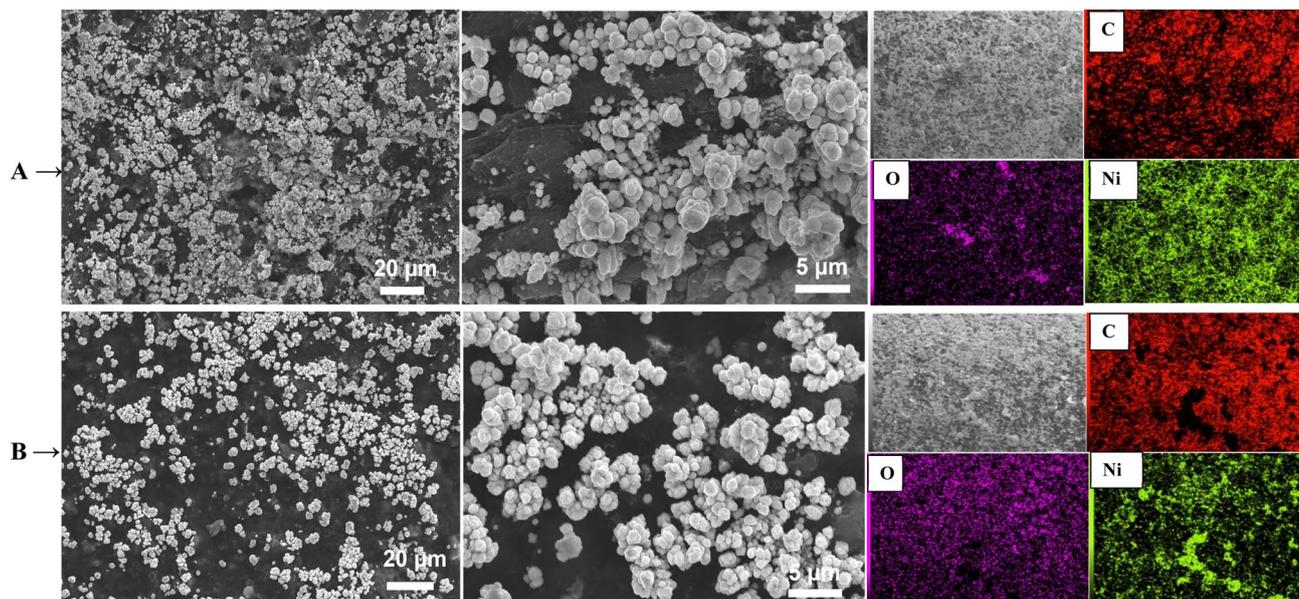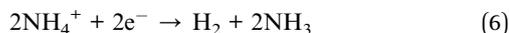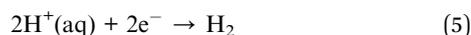
$$M^{n+}(aq) + ne^- \rightarrow M(s) \tag{4}$$
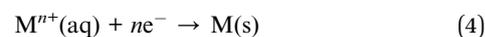
Fig. 3 SEM images with different magnifications elemental mapping EDX analysis of (A) Ni(OH)$_2$/RGR electrode, and (B) Ni(OH)$_2$/FEGR electrode.

$$2H^+(aq) + 2e^- \rightarrow H_2 \qquad (5)$$

$$2NH_4^+ + 2e^- \rightarrow H_2 + 2NH_3 \qquad (6)$$

So, the coagulation nature of the prepared film of the catalyst layer can be minimized by increasing the rate of hydrogen evolution at the expense of the metal deposition. During the deposition of Ni(OH)$_2$/RGR and Ni(OH)$_2$/FEGR, a controlled amount of charge (20 C) is allowed to pass. The presence of more functional groups over graphene layers, and grooves enhance the rate of electrolysis, and this is obvious from Fig. 2B. The number of Columbus passed during electrolysis with the time is displayed in Fig. 2B. As shown, the time needed to prepare the Ni(OH)$_2$ film on the surface of FEGR is shorter than that needed for deposition on the surface of RGR. This confirms the enhancement of the electrolysis rate. That is, the number of
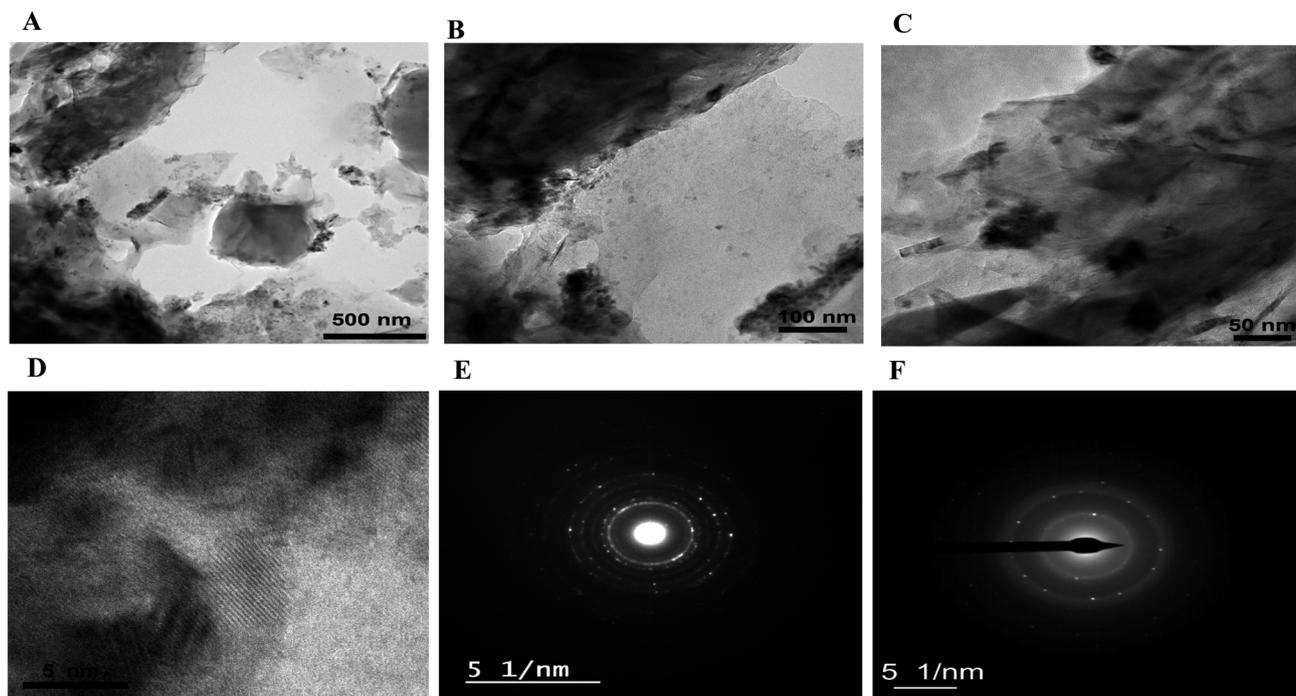

Fig. 4 HR-TEM images of Ni(OH)$_2$/FEGR electrode with different magnifications (A–D). The corresponding SAED pattern of: (E) Ni(OH)$_2$, and (F) graphene layers.

Columbus consumed for the evolution of hydrogen on the FEGR support increased more than that on the RGR support which led to the better distribution of deposited $Ni(OH)_2$ on the surface of FEGR support (*c.f.* Fig. 3).

Firstly, in this regard, ICP measurements are carried out to confirm that the consumed amount of Columbus for hydrogen evolution increased on FEGR. The amounts of electrodeposited $Ni(OH)_2$ on the FEGR and RGR are 0.7 and 1.3 mg, respectively. Secondly, from mapping EDX (Fig. 3), the mass percentage of Ni obtained on the surface of FEGR support (12.64%) is less than that on the RGR support (31.59%) which is consistent with ICP analysis. Additionally, the mass percentage of elemental oxygen of FEGR, $Ni(OH)_2/RGR$, and $Ni(OH)_2/FEGR$ is 26.92%, 6.04%, and 12.64%, respectively. The high O% on the surface of the FEGR is a result of the exfoliation step during its preparation.[21] On the other hand, a noticeable decrease of O% on $Ni(OH)_2/$ RGR, and $Ni(OH)_2/FEGR$ electrodes is due to the coverage of $Ni(OH)_2$ on the surface of the support.

Furthermore, from Fig. 3A and B, $Ni(OH)_2$ on both RGR and FEGR electrodes, respectively, displays spherical nanoparticle morphology. But the distribution of these spherical nanoparticles on the FEGR is in a homogeneous uniform matter which is better than that on the RGR as depicted from SEM and mapping EDX analysis (see Fig. 3A and B). Moreover, the HR-TEM analysis of the $Ni(OH)_2/FEGR$ electrode as the best one towards GOR (*c.f.* Fig. 8 and 9) is displayed in Fig. 4. HR-TEM is performed to highlight the morphology and investigate the crystalline structure of the proposed catalyst. As shown in Fig. 4A, the TEM image of $Ni(OH)_2/FEGR$ agrees with the morphology obtained from the SEM analysis. Also, from images with high magnifications (Fig. 4B and C), we can safely conclude

that the spherical nanoparticles of $Ni(OH)_2$ are deposited on the exfoliated graphene layers. Importantly, Fig. 4D displays the lattice fringes that confirms the crystalline nature of the $Ni(OH)_2$ active particles. Additionally, Fig. 4E displays the selected area electron diffraction (SAED) of $Ni(OH)_2$ active particles. The bright spots around the ring indicate the polycrystalline nature of the $Ni(OH)_2$. The measured d-spacing values from the obtained rings in Fig. 4E are 7.6, 4.6, 3.9, and 2.3 Å. While the *d*-spacing values of 7.6 and 3.9 Å are nearly equal to the values corresponding to α-$Ni(OH)_2$ (JCPDS No. 41–1424),[46,47] the values of 4.6 and 2.3 Å indicate the presence of some facets of β-$Ni(OH)_2$ (JCPDS No. 14–0117).[46,48] So, one can conclude that $Ni(OH)_2$ is electrodeposited with mixed α-, and β-phases that is further confirmed by the XRD analysis (*c.f.* Fig. 6). Moreover, Fig. 4F displays the SAED pattern of selected regions of metal-free graphene layers. From Fig. 4F, the obtained ring that contains bright spots displays a *d*-spacing value of 2.5 Å confirming the presence of graphene layers.[49,50]

XPS analyses are carried out to investigate the oxidation states of Ni in RGR and FEGR electrodes. From the enlarged view of Ni 2p of both electrodes, as shown in Fig. 5A and D, the observed peaks at binding energies around 856 and 873 eV confirm that Ni is present as $Ni(OH)_2$. Also, the presence of the two satellite peaks at binding energies of 861 and 880 eV confirms the formation of $Ni(OH)_2$.[51–55] Additionally, from the deconvoluted O 1s spectra of both $Ni(OH)_2/RGR$ and $Ni(OH)_2/$ FEGR electrodes, Fig. 5B and E, the main peak around 531 eV confirms the formation of nickel hydroxide.[51] By comparing the other peaks of the O 1s of both electrodes, $Ni(OH)_2/RGR$ displays two other peaks for C–OH and adsorbed H_2O. The $Ni(OH)_2/FEGR$ electrode displays four other peaks for C–OH,
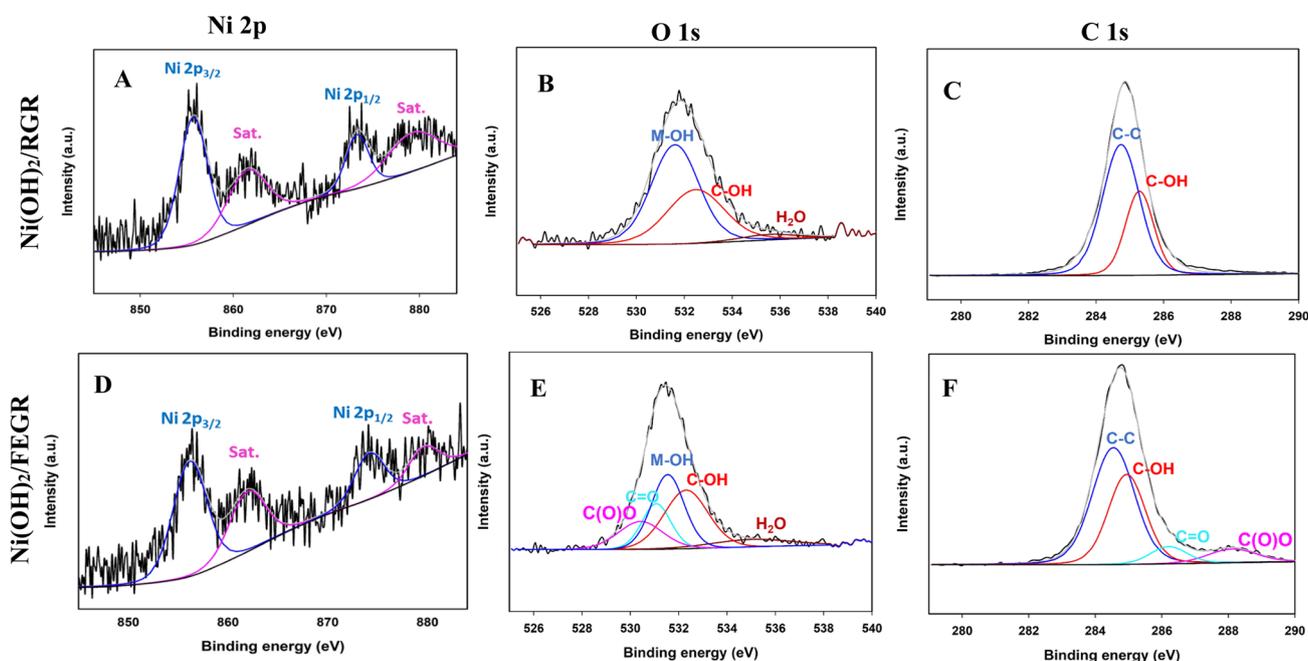

Fig. 5 XPS spectra of (A) Ni 2p, (B) O 1s, and (C) C 1s for $Ni(OH)_2/RGR$ electrode. XPS spectra of (D) Ni 2p, (E) O 1s, and (F) C 1s for $Ni(OH)_2/FEGR$ electrode.
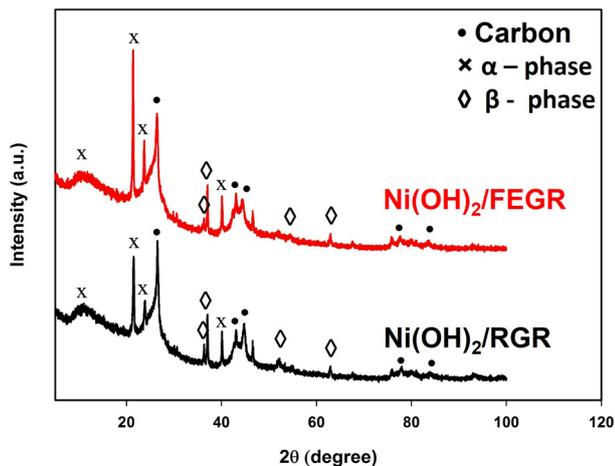
Fig. 6 XRD patterns of Ni(OH)$_2$/RGR (black line), and Ni(OH)$_2$/FEGR (red line) electrodes.

C(O), C(O)O, and adsorbed H$_2$O. The presence of the C(O), C(O)O peaks in the Ni(OH)$_2$/FEGR electrodes that do not exist in the Ni(OH)$_2$/RGR electrode is due to the oxidation which occurred during the preparation of the FEGR support, the electro exfoliation step.[21] Moreover, the oxygenated functional groups that exist in the C 1s spectra of both electrodes, as shown in Fig. 5C and F, which is consistent with the O 1s spectra (Fig. 5B and E).[21,54] The occurrence of more oxygenated functional groups on the surface of the Ni(OH)$_2$/FEGR consistency with the elemental mapping EDX analysis of Ni(OH)$_2$/FEGR displays higher oxygen percentage compared to the Ni(OH)$_2$/RGR.

Also, the XRD analyses are carried out to investigate the phase of Ni(OH)$_2$. XRD patterns of the as-prepared electrodes, *i.e.*, Ni(OH)$_2$/RGR and Ni(OH)$_2$/FEGR are depicted in Fig. 6. Both electrodes are composed of mixed phases (alpha and beta). While the corresponding peaks of β-Ni(OH)$_2$ were observed at 36°, 37°, 52°, and 63° (JCPDS No. 14–0117),[46,48] the corresponding peaks of α-Ni(OH)$_2$ appeared at 12°, 21°, 23°, and 40°

(JCPDS No. 41–1424).[46,47] Additionally, peaks due to the hexagonal graphitic structure of RGR and FEGR support are detected around 2θ of 25°, 42°, 43°, 77°, and 83°.[56,57]

As predicted from the physical analysis of both Ni(OH)$_2$/RGR and Ni(OH)$_2$/FEGR electrodes, Ni(OH)$_2$/FEGR has unique properties that promote the catalytic activity toward GOR. Fig. 7A displays the CVs of the prepared electrodes that show characteristic redox peaks within the selected potential window resulting from the transformation of the α- and β-Ni–OH to β- and γ-Ni–OOH, respectively. The position of the peaks on the CV indicates that the transformation of Ni(OH)$_2$ to NiOOH is a diffusion-controlled process.[2,21] To confirm that this transformation is a diffusion-controlled process, the study of the effect of potential scan rate (v) on the current peak (I_p) was done. By plotting I_p against the $v^{0.5}$ (see Fig. 7B), a linear relation is obtained with R^2 equals 0.9999 which confirms that the transformation of the Ni(OH)$_2$ to NiOOH is a diffusion-controlled process.[58,59] The large difference in CVs currents between the Ni(OH)$_2$/RGR, and Ni(OH)$_2$/FEGR indicates that the Ni(OH)$_2$/FEGR possesses a higher electrochemical active site on its surface than Ni(OH)$_2$/RGR electrode that in turn contributes larger in the electrocatalysis of glucose oxidation with greater extent. As mentioned above the higher capacity of the Ni(OH)$_2$/FEGR is due to (i) the FEGR support providing a large surface area to accommodate a large number of active sites on its surface, (ii) the presence of the grooves and oxygenated functional groups enhances the rate and the consumed amount of the hydrogen evolution that prevent the coagulation of catalyst' active sites on the surface of the substrate, and (iii) the presence of exfoliated graphene layers that enhance the electronic conductivity. To confirm that the active sites are well distributed on the surface of the FEGR support electrochemically, the following relation (eqn (7)) was used:

$$q = q_\infty + av^{-0.5} \tag{7}$$

where q is the charge in Coulombs estimated at various potential scan rates in CV, q_∞ is the maximum amount of the
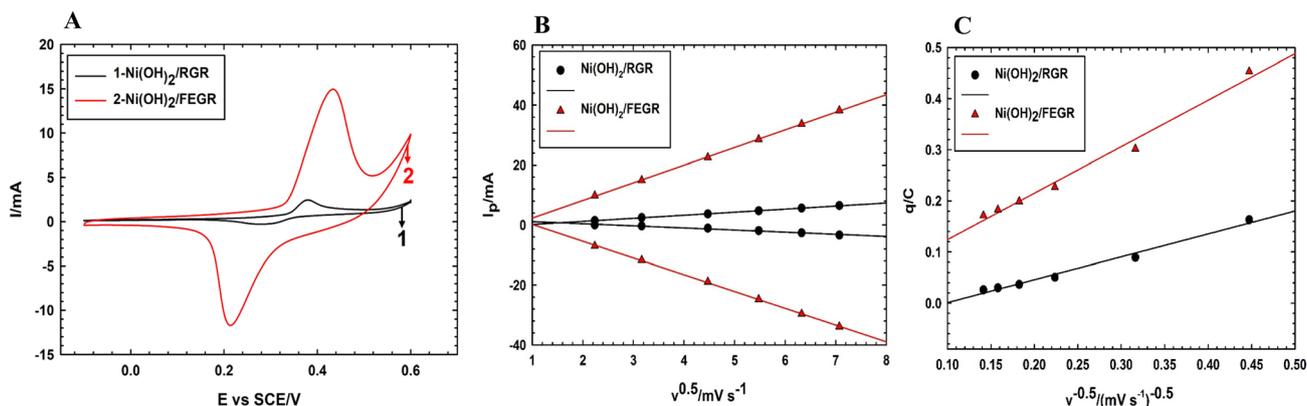
Fig. 7 (A) CVs of Ni(OH)$_2$/RGR, and (B) Ni(OH)$_2$/FEGR electrodes measured in 0.5 M NaOH solution at a potential scan rate of 10 mV s^{-1}. (B) The variation of anodic and cathodic peaks current with the square root of potential scan rate ($v^{0.5}$) for Ni(OH)$_2$/RGR, and Ni(OH)$_2$/FEGR electrodes measured in 0.5 M NaOH solution. (C) The variation of q with the reciprocal of the square root of the potential scan rate ($v^{-0.5}$) measured in 0.5 M NaOH solution.
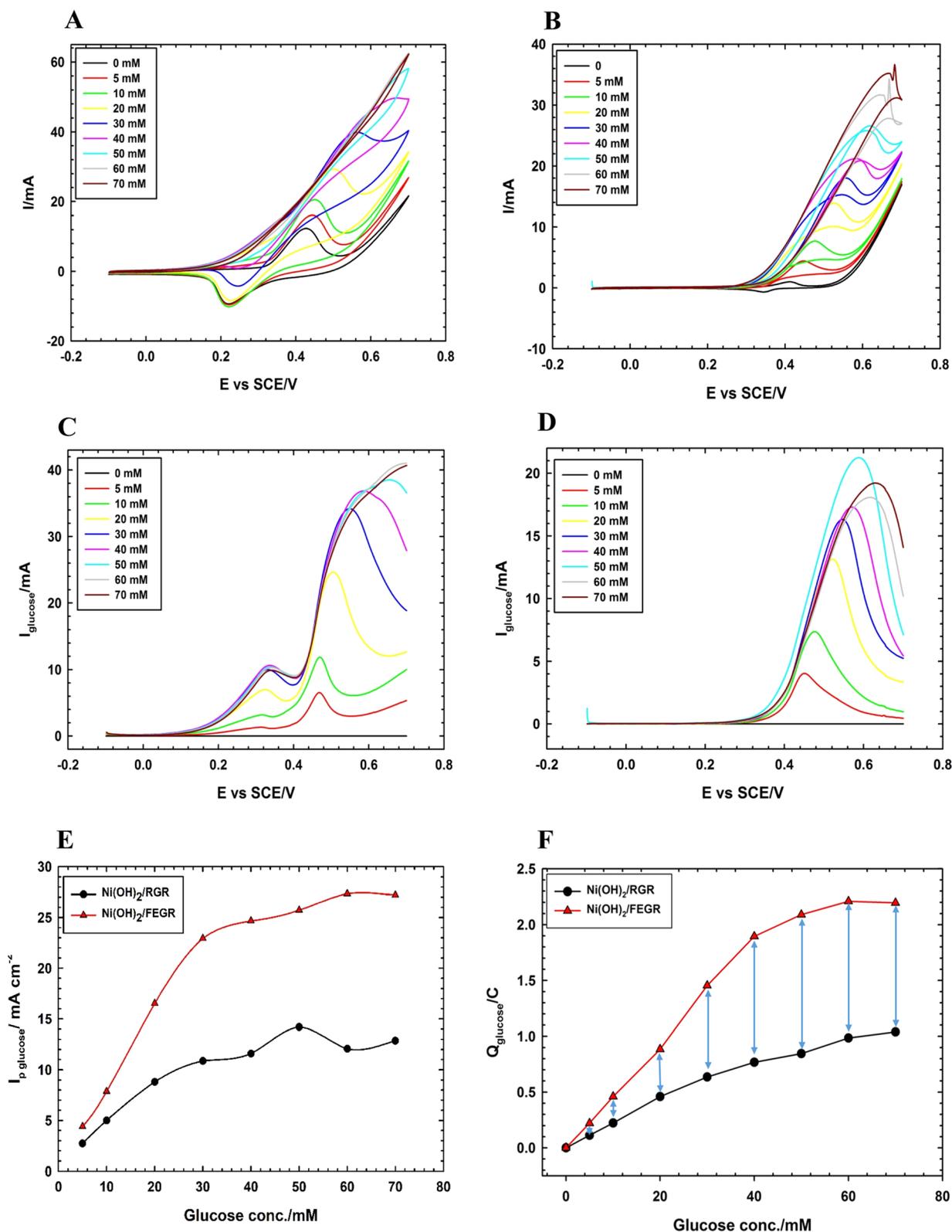
Fig. 8 CVs of (A) Ni(OH)$_2$/FEGR, and (B) Ni(OH)$_2$/RGR electrodes. LSVs of (C) Ni(OH)$_2$/FEGR and (D) Ni(OH)$_2$/RGR electrodes. (E) Variation of peak current due to glucose oxidation with the used glucose concentration at Ni(OH)$_2$/FEGR (red line) and Ni(OH)$_2$/RGR (black line) electrodes. (F) Variation of the amount of Columbus due to glucose oxidation with the used glucose concentration at Ni(OH)$_2$/FEGR (red line) and Ni(OH)$_2$/RGR (black line) electrodes. Note that: all measurements were operated in 0.5 M NaOH solution containing various concentrations of glucose (0, 5, 10, 20, 30, 40, 50, 60, and 70 mM) at a potential scan rate of 10 mV s^{-1}.

Table 1   Comparison between the electrocatalytic activity of Ni(OH)$_2$/RGR and Ni(OH)$_2$/FEGR electrodes towards GOR

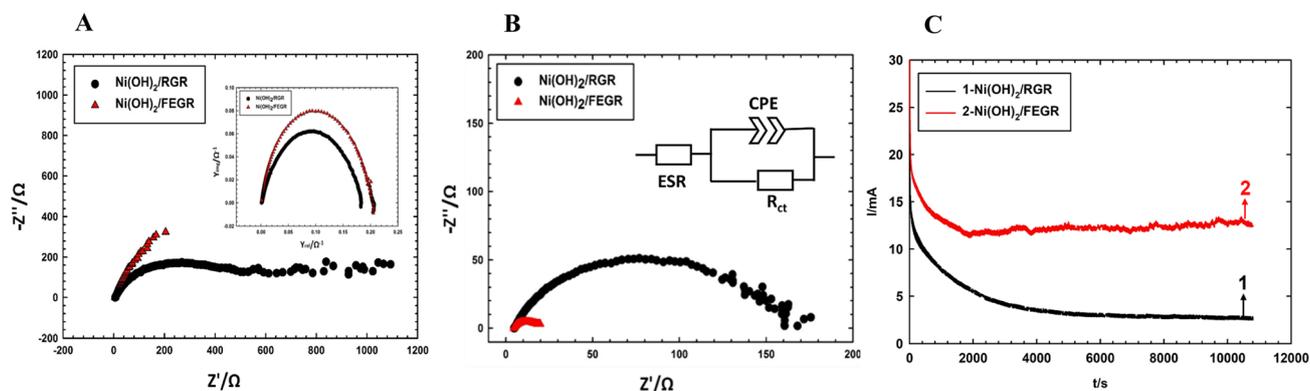|	Ni(OH)$_2$/RGR			Ni(OH)$_2$/FEGR		
Glucose conc.	I_p/mA cm^{-2}	I_p/A g^{-1}	Q/mC	I_p/mA cm^{-2}	I_p/A g^{-1}	Q/mC
5	2.73	3	112.5	4.4	9.3	220.6
10	5	5.6	223	7.9	16.7	459.9
20	8.8	9.9	459.5	16.5	35.1	884.7
30	10.9	12.2	636.3	22.9	48.6	1453.9
40	11.6	13	767.8	24.7	52.3	1894.6
50	14.2	15.9	845.3	25.7	54.6	2089.7
60	12.1	13.6	985	27.3	58	2209.9
70	12.9	14.4	103.9	27.2	57.7	2196.1

Fig. 9   (A) Nyquist plots of Ni(OH)$_2$/RGR (black line) and Ni(OH)$_2$/FEGR (red line) electrodes at OCP and their insets admittance plots of Ni(OH)$_2$/RGR (black line) and Ni(OH)$_2$/FEGR (red line) electrodes measured in 0.5 M NaOH solution. (B) Nyquist plots of Ni(OH)$_2$/RGR (black line) and Ni(OH)$_2$/FEGR (red line) electrodes measured in 0.5 M NaOH solution containing 30 mM glucose at 0.3 V *vs.* SCE. (C) Chronoamperograms for GOR were obtained at Ni(OH)$_2$/RGR (black line) and Ni(OH)$_2$/FEGR (red line) electrodes measured in 0.5 M NaOH solution containing 30 mM glucose at 0.55 V for 3 h.

charge related to the "outer" surface of active material, a is a constant, and ν is the potential scan rate (mV s^{-1}) (see Fig. 7C).[2,60] The value of the intercept of Ni(OH)$_2$/FEGR is much greater than that of Ni(OH)$_2$/RGR. So, Ni(OH)$_2$/FEGR has active sites 77.4 times more than Ni(OH)$_2$/RGR indicating that GOR will be catalyzed by a great extent on the surface of Ni(OH)$_2$/FEGR due to the large available number of active sites of a catalyst with good and uniform distribution.

As indicated in Fig. 8A and B, the GOR is markedly enhanced on the surface of the Ni(OH)$_2$/FEGR electrode compared with Ni(OH)$_2$/RGR electrode. Ni(OH)$_2$/FEGR has a larger current than Ni(OH)$_2$/RGR and this is attributed to the accessibility of the large active sites to oxidize a large number of glucose molecules. Although the Ni(OH)$_2$/FEGR electrode has a lower loading amount of Ni than that of the Ni(OH)$_2$/RGR electrode as indicated above from ICP measurements and mapping EDX analysis, the Ni(OH)$_2$/FEGR has a higher degree of efficiency toward the GOR due to possessing a high number of available active sites that distributed homogeneously with a low degree of coagulation compared to Ni distribution in case of Ni(OH)$_2$/RGR electrode. Importantly from the reduction peaks of both electrodes after the oxidation of glucose, the reduction peak of Ni(OH)$_2$/RGR disappears in comparison with its blank due to all active sites (small active sites due to the coagulation nature of

the prepared catalyst) are consumed during the GOR. On the other hand, the reduction peak of Ni(OH)$_2$/FEGR is minimized at a small concentration of glucose and disappears at high glucose concentration in comparison with its blank which confirms that there is an excess of active sites that contribute to the glucose oxidation more at high glucose concentration. Fig. 8C and D displayed the resulting current due to glucose oxidation only by subtracting the total current (current due to the transformation of the α- and β-Ni–OH to β- and γ-Ni–OOH and glucose oxidation) from the blank current (current due to the transformation of α- and β-Ni–OH to β- and γ-Ni–OOH only). Table 1 summarizes the results of Fig. 8C and D. Peak current due to glucose oxidation at the surface of Ni(OH)$_2$/FEGR is higher than Ni(OH)$_2$/RGR and the difference between current peaks increased by increasing glucose oxidation which confirms there is a more oxidation degree for glucose at higher concentration due to the more contribution of active sites of Ni(OH)$_2$/FEGR catalyst (see Fig. 8E). From Fig. 8F, by comparing the degree of oxidation of glucose over the selected potential window, the amount of Columbus relating due to the oxidation of glucose at the surface of the Ni(OH)$_2$/FEGR is higher than that of Ni(OH)$_2$/RGR and displays the same trend of the Fig. 8E confirms more oxidation of glucose molecules at the surface of the Ni(OH)$_2$/FEGR. The number of glucose molecules oxidized
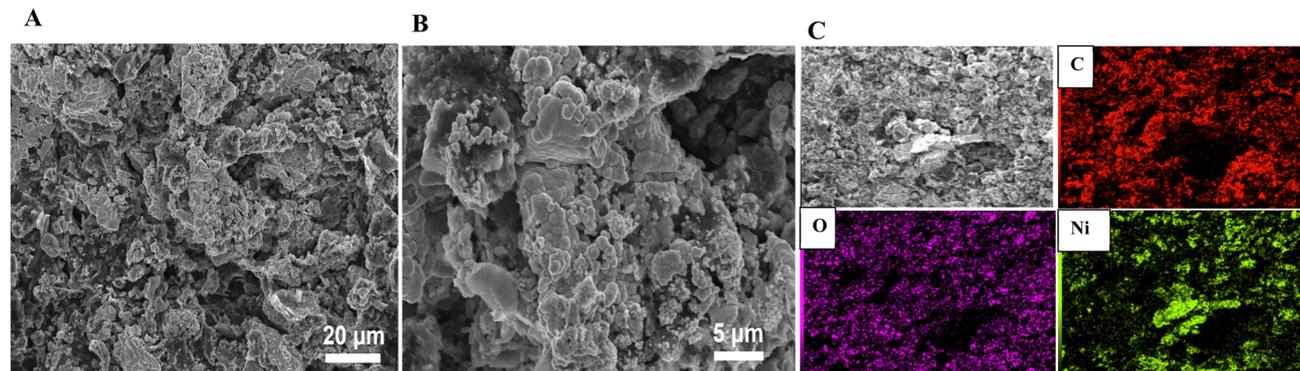
Fig. 10 SEM images of Ni(OH)$_2$/FEGR after GOR long-term operation for 3 h of continuous operation at 0.55 V measured in 0.5 M NaOH solution containing 30 mM glucose at different magnifications (A and B). (C) The corresponding elemental mapping-EDX analysis of Ni(OH)$_2$/FEGR electrode.

Table 2 Comparison between Ni(OH)$_2$/FEGR catalyst and other Ni-based catalysts toward GOR

Material	Supporting electrolyte	Glucose	Current density (mA cm^{-2})	Scan rate (mV s^{-1})	Onset potential (mV) vs. SCE	Ref.
Ni$_4$CO$_2$/AC	3 M KOH	1 M	77	10	229	17
Ni–Co-rGO	3 M KOH	1 M	13.5	50	211	66
NiO$_x$/MnO$_x$/GNs/GC	0.5 M NaOH	20 mM	170	100	320	67
Nano Ni/Ti	0.5 M NaOH	10 mM	29	10	410	68
Nano NiO$_x$/GC	0.3 M KOH	10 mM	12	100	330	69
NiCuO/ITO	1 M KOH	30 mM	0.425	100	105	70
NiO$_x$/MnO$_x$/GC	0.5 M NaOH	20 mM	14	100	266	71
Ni$_6$/AB	0.1 M KOH	5 mM	2.5	10	241	72
NiFe$_2$O$_4$/GC	0.5 M NaOH	60 mM	0.29	200	292	73
Ni(OH)$_2$/FEGR	0.5 M NaOH	30 mM	22.9	10	180	This work

per catalytic active sites is defined as the turnover number (TON). TON is directly proportional to the current (at specific potential) produced due to fuel oxidation per number of active sites of the prepared catalyst.[61,62] It is found that the TON of Ni(OH)$_2$/FEGR at 0.55 V is two times the TON of Ni(OH)$_2$/RGR which is consistent with the above results.

Moreover, Ni(OH)$_2$/FEGR has a lower onset potential (0.18 V vs. SCE) than that of Ni(OH)$_2$/RGR (0.3 V) and this is mainly due to an increase in the electronic conductivity of the prepared electrode. The electronic conductivity of the Ni(OH)$_2$/FEGR is higher than that of the Ni(OH)$_2$/RGR due to the presence of exfoliated graphene layers. Exfoliation delivers the electron very fast to the surface of the active material and facilitates the transformation of Ni(OH)$_2$ to NiOOH that in turn oxidizes glucose to gluconolactone according to eqn (1) and (2). To confirm that the Ni(OH)$_2$/FEGR has a higher electronic conductivity, the EIS measurements firstly at open circuit potential were performed. The Nyquist plots are displayed in Fig. 9A and it is clear that the electrochemical equivalent series resistance (ESR) for the Ni(OH)$_2$/FEGR is smaller than that of Ni(OH)$_2$/RGR indicating that the Ni(OH)$_2$/FEGR has a higher electronic conductivity.[21,63,64] Also, Ni(OH)$_2$/FEGR has a more vertical line compared to Ni(OH)$_2$/RGR which confirms that the Ni(OH)$_2$/FEGR has a higher capacity value than Ni(OH)$_2$/RGR

due to the uniform distribution of a large number of active sites on the surface of the FEGR support as mentioned above and concluded from CVs of both electrodes.[65] Additionally, the admittance plot, see inset of Fig. 9A, displayed an increment consistent with the ESR because the admittance, as known, is the inverse of the impedance. So, the GOR is expected to have a lower charge transfer resistance on the surface of Ni(OH)$_2$/FEGR than Ni(OH)$_2$/RGR. Clearly, from the Nyquist plots operated in the presence of 30 mM glucose for both electrodes at 0.3 V vs. SCE (Fig. 9B) and the data resulting from the fitted equivalent circuit (see inset of Fig. 9B), the charge transfer resistance on the surface of Ni(OH)$_2$/FEGR (15 Ohm) is much lower than that of the Ni(OH)$_2$/RGR (157 Ohm) which reflected the lower onset potential of the Ni(OH)$_2$/FEGR compared to Ni(OH)$_2$/RGR. Not only the onset potential and I_p are factors that are enhanced on the surface of the Ni(OH)$_2$/FEGR but also the durability of the prepared electrode is outstanding compared to that of the Ni(OH)$_2$/RGR. From Fig. 9C, both electrodes start displaying a large decaying in the response to the gain current and this is due to the oxidation of a large number of glucose molecules near the surface of both electrodes. But Ni(OH)$_2$/RGR continues to decay compared with the Ni(OH)$_2$/FEGR that displays superb durability by showing a constant current response with time for about 3 h. The

excellent stability of the Ni(OH)$_2$/FEGR may be attributed to the strong interaction between the Ni(OH)$_2$ and FEGR support throughout oxygen functional groups. Additionally, the persistence of morphology of the Ni(OH)$_2$ active particles after continuous operation for 3 h towards GOR reveals the robustness and insignificant distortion of the catalyst reflecting the remarkable stability of the catalyst (see Fig. 10A and B). From Fig. 10A and B, the Ni(OH)$_2$ active particles have the same morphology (nanosphere) as before the long-term stability operation. Moreover, the active particles are still uniformly distributed over the exfoliated graphene layers (see Fig. 10C). As a general conclusion, the Ni(OH)$_2$/FEGR has a premium catalytic performance than the Ni(OH)$_2$/RGR due to: (i) the ionic conductivity is increased by making the most active sites available for ease of interaction with hydroxide ions and hence oxidation of glucose, and (ii) the electronic conductivity is also increased that in turn delivers the electron very fast to active sites and hence glucose molecules are oxidized efficiently. Additionally, the prepared catalyst is a promising catalyst due to its facile preparation *via* partial electrochemical exfoliation that led to the formation of graphene layers easily without any binder or using any harsh chemicals used in the preparation of catalyst-based graphene support applied toward glucose oxidation. Moreover, the prepared catalyst is an excellent catalyst for GOR compared to other reported catalysts (see Table 2).

4. Conclusion

Ni(OH)$_2$ active material is deposited on *in situ* generated FEGR. FEGR support enhanced GOR by increasing the ionic conductivity of Ni(OH)$_2$ *via* providing a large activated surface area (26 times than RGR) that is characterized by defective surface, high oxygenated surface functional groups, and exfoliated graphene layers. In addition, FEGR increases the hydrogen evolution reaction during the cathodic electrodeposition of Ni resulting in a better distribution of active material. Ionic conductivity is reflected in the high peak current due to the oxidation of a large number of glucose molecules even if Ni(OH)$_2$/FEGR has a low mass loading compared to Ni(OH)$_2$/RGR. Also, the electronic conductivity contributes to the increment of peak current by delivering the electrons very fast to the active material which transfers a large number of Ni(OH)$_2$ to NiOOH in a short time and hence oxidizes a large number of glucose molecules. Additionally, the electronic conductivity plays an important role in the oxidation of glucose at a lower onset potential (120 mV lower than Ni(OH)$_2$/RGR). The exfoliated graphene layers increase the electronic conductivity of the prepared Ni(OH)$_2$/FEGR electrode (as revealed by EIS measurements) which in turn assists the oxidation at lower overpotential. Moreover, the FEGR support boosted the stability of Ni(OH)$_2$ toward the GOR reaction by supplying a constant current for a long time of electrolysis.

Conflicts of interest

There are no conflicts to declare.

References

1 M. Bahari, M. A. Malmberg, D. M. Brown, S. H. Nazari, R. S. Lewis, G. D. Watt and J. N. Harb, *Appl. Energy*, 2020, **261**, 114382.

2 A. M. Abdelrahim, M. G. Abd El-Moghny, M. E. El-Shakre and M. S. El-Deab, *Electrochim. Acta*, 2021, **378**, 137991.

3 A. H. Abu-Ghazala, H. H. Abdelhady, A. A. Mazhar and M. S. El-Deab, *Renewable Energy*, 2022, **200**, 1120–1133.

4 Y. Liu, C. Liu, X. Yu, H. Osgood and G. Wu, *Phys. Chem. Chem. Phys.*, 2017, **19**, 330–339.

5 O. A. Mawlid, H. H. Abdelhady and M. S. El-Deab, *Energy Convers. Manage.*, 2022, **273**, 116435.

6 A. Khoobi and M. Salavati-Niasari, *Energy*, 2019, **178**, 50–56.

7 H. Bensalah, S. A. Younssi, M. Ouammou, A. Gurlo and M. F. Bekheet, *J. Environ. Chem. Eng.*, 2020, **8**, 103807.

8 Y. Chen, K. P. Prasad, X. Wang, H. Pang, R. Yan, A. Than, M. B. Chan-Park and P. Chen, *Phys. Chem. Chem. Phys.*, 2013, **15**, 9170–9176.

9 M. Irfan, I. U. Khan, J. Wang, Y. Li and X. Liu, *RSC Adv.*, 2020, **10**, 6444–6451.

10 Y. Xin, F. Wang, L. Chen, Y. Li and K. Shen, *Green Chem.*, 2022, **24**, 6544–6555.

11 W.-J. Liu, Z. Xu, D. Zhao, X.-Q. Pan, H.-C. Li, X. Hu, Z.-Y. Fan, W.-K. Wang, G.-H. Zhao and S. Jin, *Nat. Commun.*, 2020, **11**, 1–11.

12 M. R. Rizk, M. G. Abd El-Moghny, A. Mazhar, M. S. El-Deab and B. E. El-Anadouli, *Sustainable Energy Fuels*, 2021, **5**, 986–994.

13 A. M. Abdelrahim, M. G. Abd El-Moghny, M. E. El-Shakre and M. S. El-Deab, *Electrochim. Acta*, 2023, **440**, 141726.

14 G. A. El-Nagar, I. Derr, A. Fetyan and C. Roth, *Appl. Catal., B*, 2017, **204**, 185–199.

15 R. Fu, Y. Lu, Y. Ding, L. Li, Z. Ren, X. Si and Q. Wu, *Microchem. J.*, 2019, **150**, 104106.

16 S. Kukunuri, M. R. Krishnan and S. Sampath, *Phys. Chem. Chem. Phys.*, 2015, **17**, 23448–23459.

17 M. Gao, X. Liu, M. Irfan, J. Shi, X. Wang and P. Zhang, *Int. J. Hydrogen Energy*, 2018, **43**, 1805–1815.

18 A. Eshghi, *Int. J. Hydrogen Energy*, 2017, **42**, 15064–15072.

19 M. A. Goda, M. G. Abd El-Moghny and M. S. El-Deab, *J. Electrochem. Soc.*, 2020, **167**, 064522.

20 Y. Wu, X. Yang, S. Liu, Y. Xing, J. Peng, Y. Peng, G. Ni and X. Jin, *RSC Adv.*, 2020, **10**, 39447–39454.

21 A. M. Abdelrahim, M. G. Abd El-Moghny and M. S. El-Deab, *RSC Adv.*, 2021, **11**, 26258–26272.

22 T. Nguyen, M. Boudard, M. J. Carmezim and M. F. Montemor, *Sci. Rep.*, 2017, **7**, 1–10.

23 L. Liu, Y. Hou, Y. Gao, N. Yang, J. Liu and X. Wang, *Electrochim. Acta*, 2019, **295**, 340–346.

24 G.-X. X. Tong, F.-T. T. Liu, W.-H. H. Wu, J.-P. P. Shen, X. Hu and Y. Liang, *CrystEngComm*, 2012, **14**, 5963–5973.

25 P. Lu, Y. Lei, S. Lu, Q. Wang and Q. Liu, *Anal. Chim. Acta*, 2015, **880**, 42–51.

26 J. Xing, S. Wu and K. Y. S. Ng, *RSC Adv.*, 2015, **5**, 88780–88786.

27 X. L. Shilei Xie, S. I. Liu and F. Cheng, *ChemElectroChem*, 2108, **5**, 571–582.

28 Y. Song, T. Liu, F. Qian, C. Zhu, B. Yao, E. Duoss, C. Spadaccini, M. Worsley and Y. Li, *J. Colloid Interface Sci.*, 2018, **509**, 529–545.

29 C. J. Raj, R. Manikandan, W. G. Lee, W. J. Cho, K. H. Yu and B. C. Kim, *Electrochim. Acta*, 2018, **283**, 1543–1550.

30 D. Wei, L. Grande, V. Chundi, R. White, C. Bower, P. Andrew and T. Ryhänen, *Chem. Commun.*, 2012, **48**, 1239–1241.

31 M. E. Ghaith, M. G. Abd El-Moghny, G. A. El-Nagar, H. H. Alalawy, M. E. El-Shakre and M. S. El-Deab, *RSC Adv.*, 2023, **13**, 895–905.

32 S. Yang, M. R. Lohe, K. Müllen and X. Feng, *Adv. Funct. Mater.*, 2016, **28**, 6213–6221.

33 Y. Song, D. Y. Feng, T. Y. Liu, Y. Li and X. X. Liu, *Nanoscale*, 2015, **7**, 3581–3587.

34 H. Y. Li, Y. Yu, L. L. Liu, L. L. Liu and Y. Wu, *Electrochim. Acta*, 2017, **228**, 553–561.

35 Y. Song, J. L. Xu and X. X. Liu, *J. Power Sources*, 2014, **249**, 48–58.

36 J. Hou, Y. Shao, M. W. Ellis, R. B. Moore and B. Yi, *Phys. Chem. Chem. Phys.*, 2011, **13**, 15384–15402.

37 J. I. Paredes and J. M. Munuera, *J. Mater. Chem. A*, 2017, **5**, 7228–7242.

38 J. Liu, C. K. Poh, D. Zhan, L. Lai, S. H. Lim, L. Wang, X. Liu, N. Gopal Sahoo, C. Li, Z. Shen and J. Lin, *Nano Energy*, 2013, **2**, 377–386.

39 I. O. Baibars, M. G. Abd El-Moghny and M. S. El-Deab, *Electrochim. Acta*, 2022, **410**, 139992.

40 M. R. Rizk, M. G. Abd El-Moghny, H. H. Abdelhady, W. M. Ragheb, A. H. Mohamed, H. F. Fouad, M. Mohsen, A. S. Kamel and M. S. El-Deab, *Int. J. Hydrogen Energy*, 2022, **47**, 32145–32157.

41 I. O. Baibars, M. G. Abd El-Moghny and M. S. El-Deab, *J Environ Chem Eng*, 2022, **10**, 108736.

42 D. S. Hall, D. J. Lockwood, C. Bock and B. R. MacDougall, *Proc. R. Soc. A*, 2015, **471**, 20140792.

43 A. M. Abdelrahim, M. G. Abd El-Moghny, M. E. El-Shakre and M. S. El-Deab, *J Energy Storage*, 2023, **57**, 106218.

44 B. J. Plowman, L. A. Jones and S. K. Bhargava, *Chem. Commun.*, 2015, **51**, 4331–4346.

45 H. Ashassi-Sorkhabi and P. La'le Badakhshan, *Appl. Surf. Sci.*, 2017, **419**, 165–176.

46 W. He, X. Li, S. An, T. Li, Y. Zhang and J. Cui, *Sci. Rep.*, 2019, **9**, 1–8.

47 D. Yang, P. Liu, Y. Gao, H. Wu, Y. Cao, Q. Xiao and H. Li, *J. Mater. Chem.*, 2012, **22**, 7224–7231.

48 L.-J. Zhou, X. Huang, H. Chen, P. Jin, G.-D. Li and X. Zou, *Dalton Trans.*, 2015, **44**, 11592–11600.

49 P. C. Ooi, M. A. S. Mohammad Haniff, M. F. Mohd Razip Wee, B. T. Goh, C. F. Dee, M. A. Mohamed and B. Y. Majlis, *Sci. Rep.*, 2019, **9**, 1–8.

50 T. Fan, W. Zeng, W. Tang, C. Yuan, S. Tong, K. Cai, Y. Liu, W. Huang, Y. Min and A. J. Epstein, *Nanoscale Res. Lett.*, 2015, **10**, 1–8.

51 M. R. Rizk and M. G. Abd El-Moghny, *Int. J. Hydrogen Energy*, 2021, **46**, 645–655.

52 L. Hou, Y. Shi, C. Wu, Y. Zhang, Y. Ma, X. Sun, J. Sun, X. Zhang and C. Yuan, *Adv. Funct. Mater.*, 2018, **28**, 1705921.

53 H. Chen, L. Hu, M. Chen, Y. Yan and L. Wu, *Adv. Funct. Mater.*, 2014, **24**, 934–942.

54 Y. Chen, W. K. Pang, H. Bai, T. Zhou, Y. Liu, S. Li and Z. Guo, *Nano Lett.*, 2017, **17**, 429–436.

55 T.-H. Wu and B.-W. Hou, *Catal. Sci. Technol.*, 2021, **11**, 4294–4300.

56 J. Zhang, J. Chen, H. Yang, J. Fan, F. Zhou, Y. Wang, G. Wang and R. Wang, *J. Solid State Electrochem.*, 2017, **21**, 2975–2984.

57 M. Kazazi, A. R. Sedighi and M. A. Mokhtari, *Appl. Surf. Sci.*, 2018, **441**, 251–257.

58 Z. Sun, X. Cai, D. Y. Feng, Z. H. Huang, Y. Song and X. X. Liu, *ChemElectroChem*, 2018, **5**, 1501–1508.

59 Z. Wei, J. Yuan, S. Tang, D. Wu and L. Wu, *J. Colloid Interface Sci.*, 2019, **542**, 15–22.

60 Y. Wang, Z. Yin, G. Yan, Z. Wang, X. Li, H. Guo and J. Wang, *Electrochim. Acta*, 2020, **336**, 135734.

61 Y. Zhang, Y. Gu, S. Lin, J. Wei, Z. Wang, C. Wang, Y. Du and W. Ye, *Electrochim. Acta*, 2011, **56**, 8746–8751.

62 G. A. El-Nagar and C. Roth, *Phys. Chem. Chem. Phys.*, 2017, **19**, 2537–2548.

63 Y. Song, D. Y. Feng, T. Y. Liu, Y. Li and X. X. Liu, *Nanoscale*, 2015, **7**, 3581–3587.

64 Y. Xie and Y. Zhou, *J. Mater. Res.*, 2019, **34**, 2472–2481.

65 B. E. Conway, *Electrochemical supercapacitors scientific fundamentals and technological applications*, springer US, 1999.

66 M. Irfan, X. Liu, S. Li, I. U. Khan, Y. Li, J. Wang, X. Wang, X. Du, G. Wang and P. Zhang, *Renewable Energy*, 2020, **155**, 1118–1126.

67 A. M. Ahmed, S. Y. Sayed, G. A. El-Nagar, W. M. Morsi, M. S. El-Deab and B. E. El-Anadouli, *J. Electroanal. Chem.*, 2019, **835**, 313–323.

68 Q. Yi, W. Huang, W. Yu, L. Li and X. Liu, *Electroanalysis*, 2008, **20**, 2016–2022.

69 A. S. Danial, M. M. Saleh, S. A. Salih and M. I. Awad, *J. Power Sources*, 2015, **293**, 101–108.

70 M. Cao, H. Cao, W. Meng, Q. Wang, X. Bi, X. Liang, H. Yang, L. Zhang, M.-F. Lang and J. Sun, *Int. J. Hydrogen Energy*, 2021, **46**, 28527–28536.

71 S. M. El-Refaei, M. I. Awad, B. E. El-Anadouli and M. M. Saleh, *Electrochim. Acta*, 2013, **92**, 460–467.

72 X. Gao, W. Feng, Y. Xu, Y. Jiang, C. Huang, Y. Yi, A. Guo, X. Qiu and W. Chen, *Nanoscale Res. Lett.*, 2020, **15**, 1–9.

73 F. A. Mohammed, M. M. Khalaf, I. M. A. Mohamed, M. M. Saleh and H. M. Abd El-Lateef, *Microchem. J.*, 2020, **153**, 104507.